

# 铜纳米颗粒的飞秒激光连接过程研究

廖嘉宁, 王欣达, 周兴汶, 康慧, 郭伟, 彭鹏\*

北京航空航天大学机械工程及自动化学院, 北京 100191

**摘要** 采用飞秒激光对铜离子前驱体薄膜进行激光直写, 原位还原得到铜纳米颗粒并连接形成导电铜微结构。实验研究了激光功率对铜微结构物相成分、微观结构及导电性能的影响。进一步, 利用 COMSOL 仿真软件模拟了飞秒激光辐照下铜纳米颗粒二聚体的电场分布及温度场分布特征, 计算了不同功率单脉冲激光对铜纳米颗粒电子温度及晶格温度的影响。仿真结果表明, 激光诱导表面等离激元效应可实现对纳米颗粒的局域加热。当激光功率为 960 mW 时, 纳米颗粒热点区域的晶格温度最高为 698 K, 纳米颗粒出现表面熔化现象, 可实现颗粒间的连接。随着入射激光功率的升高, 晶格温度升高, 颗粒间连接程度提高, 与实验结果相一致。

**关键词** 激光技术; 飞秒激光; 铜纳米颗粒; 纳米连接; 界面; 局域温度

中图分类号 TN249

文献标志码 A

doi: 10.3788/CJL202148.0802008

## 1 引言

纳米材料由于其特有的表面效应及尺寸效应, 较块状材料而言, 展现出优异的机械、光学、电学、催化性能, 在信息电子、环境监测、能源生产及存储等领域具有极大应用前景<sup>[1-2]</sup>。其中, 铜(Cu)纳米颗粒作为一种互连材料, 由于其低廉的成本和类似贵金属的电导率, 受到了人们的广泛关注。通过实现铜纳米颗粒间的微尺度连接, 可优化所制备微结构的电学及光学连接性, 显著提高其电导率和机械性能, 为实现功能电子器件的高集成密度及小型化提供可能<sup>[3-4]</sup>。目前, 传统的焊接工艺如钎焊<sup>[5]</sup>、电阻点焊<sup>[6]</sup>等同样适用于纳米材料的连接, 可获得具有完整结构及良好性能的纳米单元。但是这些传统方法具有较高的热量输入, 在制造更微小精密的微电子元件时可能会对纳米结构其他部位造成过度损伤。发展低温乃至室温下的纳米材料互连技术成为人们关注的焦点。

与其他纳米连接技术相比, 激光诱导纳米连接具有高精度、低损伤、高效率等优势, 被广泛应用于航空航天、微电子器件及医疗领域<sup>[7-8]</sup>。其中, 飞秒

激光的脉冲宽度极短, 峰值功率较高, 在与材料相互作用过程中, 电子吸收光子迅速到达较高温度而晶格仍保持冷态, 热效应较小, 使得纳米材料在加工过程中展现出局部熔化特征, 有望成为制备纳米器件的新型连接技术<sup>[9-10]</sup>。Roth 等<sup>[11]</sup>采用飞秒激光诱导还原氧化铜纳米颗粒, 成功制备具有良好电导率的铜微结构( $2.1 \mu\Omega \cdot m$ ), 并使用该微结构实现了微加热器的应用。Huang 等<sup>[12]</sup>利用飞秒激光成功连接了银纳米颗粒, 并通过控制激光能量密度有效控制了银纳米颗粒的连接程度, 从而调控了纳米颗粒的表面等离子体共振增强效果。进一步, Huang 等<sup>[13]</sup>结合有限时域差分模拟, 证明飞秒激光辐照下银纳米颗粒的连接归因于表面等离激元效应, 在强场驱动下纳米颗粒发生烧蚀与重沉积过程, 有效填补颗粒间隙使得颗粒发生互连。在此过程中, 纳米颗粒整体形貌基本未发生改变, 与连续激光相比具有明显优越性。建立热作用模型, 对研究激光与纳米材料相互作用的机理具有重要意义。考虑到超短脉冲激光辐射能量向晶格转化不是瞬时完成, Anisimov 等<sup>[14]</sup>提出双温模型(TTM), 以描述激光与金属相互作用过程中, 电子及晶格的温度变化关

收稿日期: 2020-12-01; 修回日期: 2021-01-06; 录用日期: 2021-02-23

基金项目: 国家重点研发计划(2017YFB1104900)、国家自然科学基金(51975033)、北京市自然科学基金(3192020)

\* E-mail: ppeng@buaa.edu.cn

系。Cheng 等<sup>[15]</sup>以飞秒激光为热源,模拟了 Cu 纳米颗粒的超快熔化及再凝固过程,通过建立一维双温模型计算了不同激光能量密度下 Cu 颗粒电子及晶格的温度随时间变化关系。但该研究并未考虑 Cu 纳米颗粒间的等离激元效应所产生的局域热量。

综上所述,目前已有部分关于飞秒激光辐照还原 Cu 纳米颗粒的研究,但并未关注飞秒激光对 Cu 颗粒连接过程的影响,等离激元对颗粒局域温度的影响有待进一步计算。目前针对飞秒激光对 Cu 纳米颗粒的连接机理的研究,尤其飞秒激光热作用对 Cu 纳米颗粒的连接的影响方面研究还不充分。本文采用飞秒激光对预涂敷于柔性基体的铜离子前驱体进行激光扫描,原位还原并连接得到导电铜微结构。通过调控激光功率,分析了铜纳米颗粒还原、连接方式与微结构导电性的关系。利用 COMSOL 模拟了飞秒激光辐照下 Cu 纳米颗粒二聚体周围的电场及温度场分布特征,计算了不同激光功率辐照下 Cu 纳米颗粒二聚体的电子、晶格温度变化,进一步探究了飞秒激光对 Cu 纳米颗粒的连接机理。

## 2 实验部分

### 2.1 前驱体制备及激光扫描过程

实验所需原料包括三水硝酸铜  $[\text{Cu}(\text{NO}_3)_2 \cdot 3\text{H}_2\text{O}]$ 、聚甲基丙烯酸钠 (PMAA-Na)、聚乙烯吡咯烷酮 (PVP)。所用化学药品均为分析纯,全部购买自国药集团化学试剂有限公司。实验用水为去离子水。将一定量 PVP 水溶液 ( $0.25 \text{ g/mL}$ ,  $1200 \mu\text{L}$ ) 与 PMAA-Na(质量分数为 30%,  $1 \mu\text{L}$ ) 加入  $\text{Cu}(\text{NO}_3)_2 \cdot 3\text{H}_2\text{O}$  水溶液 ( $1.208 \text{ g/mL}$ ,  $1000 \mu\text{L}$ ) 中,混合形成铜离子溶液。将配制而成的铜离子溶液 ( $200 \mu\text{L}$ ) 均匀涂于聚碳酸酯柔性基底 (PC,  $2.5 \text{ cm} \times 5 \text{ cm}$ ) 表面,置于  $50^\circ\text{C}$  恒温干燥箱中干燥  $0.5 \text{ h}$  形成铜离子前驱体。采用飞秒激光对铜离子前驱体进行扫描,将铜离子还原并连接形成导电铜微结构。最后通过去离子水清洗试样,以除去未被激光辐照的部分。

### 2.2 仪器设备

采用蓝宝石固体飞秒激光 (Coherent, 美国, 以下简称 800 nm 飞秒激光),其激光波长为 800 nm、重复频率为 1 kHz、脉宽为 50 fs; 扫描电子显微镜 (SEM, Merlin Compact, 德国) 和透射电子显微镜 (HRTEM, JEOL 2100, 日本) 观察结构的形貌; 通过 X 射线衍射分析仪 (XRD, Bruker D8 Advance, 德国) 表征结构的成分,XRD 的测试条件为 Cu 靶,

扫描范围为  $30^\circ \sim 80^\circ$ ; 通过数字源表 (Keithley 2400, 美国) 测量所得结构的电学性能。

## 3 结果与讨论

### 3.1 激光功率对导电性能的影响

激光功率的变化将引起辐照区域激光能量密度的变化,造成铜微结构物相成分及微观结构的改变<sup>[16]</sup>,进而影响其导电性能。控制 800 nm 飞秒激光光斑直径为  $1225 \mu\text{m}$ ,扫描速度为  $3 \text{ mm/s}$ , 改变激光功率分别为  $322, 626, 960, 1240, 1690, 1880 \text{ mW}$ ,研究不同激光功率对所得铜微结构导电性能的影响。图 1 为所制备铜微结构方阻随激光功率变化曲线图。总体上,所得结构方阻随激光功率的升高呈现先下降后上升的趋势。当激光功率较低 ( $322 \text{ mW}$ ) 时,仅能从前驱体中还原出分散的 Cu 纳米颗粒,颗粒间并未实现连接,导致所得铜微结构方阻较大,约为  $34.3 \text{ M}\Omega \cdot \text{sq}^{-1}$ 。当激光功率增至  $626 \text{ mW}$  时,结构方阻由  $34.3 \text{ M}\Omega \cdot \text{sq}^{-1}$  降至  $36.6 \text{ }\Omega \cdot \text{sq}^{-1}$ ,下降约 6 个数量级。这是由于辐照区域激光能量密度增加,还原出的 Cu 含量增加,且结构中 Cu 纳米颗粒的连接比例提高,显著提高了结构的导电性。当激光功率增至  $960 \text{ mW}$  时,所制备的铜微结构方阻最低约为  $11.2 \text{ }\Omega \cdot \text{sq}^{-1}$ ,优于激光连接合成铜纳米线的导电薄膜 (约为  $20 \text{ }\Omega \cdot \text{sq}^{-1}$ )<sup>[17]</sup> 及溶液法制备的铜纳米线导电薄膜 (约为  $17 \text{ }\Omega \cdot \text{sq}^{-1}$ )<sup>[18]</sup>。本文测试了该功率下制备的铜微结构在弯折状态下的电阻变化率 [ $(R - R_0)/R_0$ ;  $R$  为弯折状态的电阻,  $R_0$  为结构初始电阻]。当弯折半径为  $2.3 \text{ cm}$  时,铜微结构电阻变化率为 2.9%,说明了所制备的铜导线具有较好的柔性。进

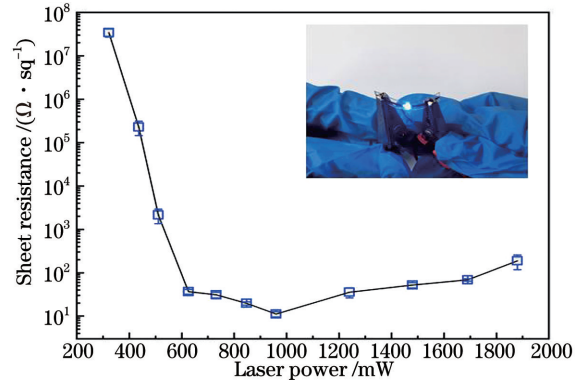


图 1 铜微结构方阻随激光功率变化曲线(插图:铜微结构所制 LED 电路数码照片)

Fig. 1 Copper microstructure sheet resistance change curve with laser power (inset: photograph of the LED circuit prepared from Cu microstructure)

一步,制备了可弯曲的LED电路,如图1插图所示。继续增加激光功率,Cu纳米颗粒间产生更强连接甚至熔化,开始出现较大球形结构,从而导致铜微结构方阻有所上升。当激光功率增至1880 mW时,铜微结构方阻增至 $187.5 \Omega \cdot \text{sq}^{-1}$ 。

### 3.2 激光功率对铜微结构物相成分及微观结构的影响

图2为飞秒激光扫描下,所得铜微结构物相成分与功率的变化关系。在不同激光功率下,铜微结构均显示为不同比例的金属Cu及Cu<sub>2</sub>O相。其中,所标识43.8°、50.9°和74.6°处的三个衍射峰分别对应于Cu的(111)、(200)和(220)面,而36.9°、42.8°和61.7°处的三个衍射峰对应于Cu<sub>2</sub>O<sup>[19]</sup>。当激光功率为322 mW时,辐照区域激光能量密度较低,仅能从前驱体中还原出分散的Cu纳米颗粒,且颗粒表面包裹较厚有机物,使得该结构主要含Cu相<sup>[20]</sup>。当激光功率升至626 mW时,Cu及Cu<sub>2</sub>O特征峰的峰强均有所增加,表明有更多Cu<sup>2+</sup>前驱体被还原为Cu<sup>+</sup>及Cu。其中,Cu<sub>2</sub>O的存在是Cu<sup>2+</sup>的不完全还原导致,当激光功率较低时,辐照区域激光能量密度低,不足以发生Cu<sup>2+</sup>的完全还原。当激光功率增至960 mW时,Cu<sub>2</sub>O相峰强最低,基本只存在Cu相,使得该功率下制备的铜微结构方阻最低。随着激光功率进一步升高,所得铜微结构中Cu特征峰下降,而Cu<sub>2</sub>O特征峰升高,这是由于激光功率过高导致还原出的Cu在大气中再次被氧化。

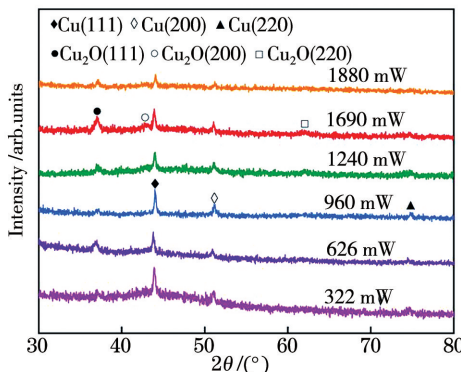


图2 不同激光功率下制备的铜微结构的XRD图

Fig. 2 XRD pattern of copper microstructure prepared with different laser powers

激光直写过程中,较低激光功率仅能实现Cu纳米颗粒的还原,颗粒间连接程度较低。随着激光功率的增加,辐照区域激光能量密度增大,还原出来的Cu纳米颗粒在激光诱导的局域“热点”作用下产生表面熔化实现互连<sup>[21]</sup>。通过对激光功率的调控,

系统研究了不同激光功率对Cu纳米颗粒连接方式的影响规律,据此深入探究了飞秒激光作用下Cu纳米颗粒的连接机理。图3为不同激光功率下所得结构的微观形貌。当激光功率较低(小于322 mW)时,仅能从前驱体中还原出分散的Cu纳米颗粒,并未实现颗粒间的连接,如图3(a)所示。当激光功率增大至626 mW时,辐照区域激光能量密度增大,可同时实现Cu纳米颗粒的还原与连接,如图3(b)所示。其中,从所得结构的局部放大图中可以看出,Cu纳米颗粒之间的间隙处发生连接。飞秒激光辐照Cu纳米颗粒时,表面等离激元效应倾向于在结构不连续处(纳米颗粒之间间隙处)聚集产生,从而导致能量输入的聚集,使得该部位能量高于其他部位,促使纳米颗粒局部熔化发生互连<sup>[22-23]</sup>。当激光功率为960 mW时,Cu纳米颗粒的连接比例及连接程度都显著提高,纳米颗粒之间基本实现了完全连接并形成均匀网状结构,其烧结颈尺寸从301 nm增加至414 nm[图3(c)],使其方阻达到最低。当激光功率增至1240 mW时,Cu纳米颗粒间产生更强连接甚至熔化,纳米颗粒的烧结颈尺寸增

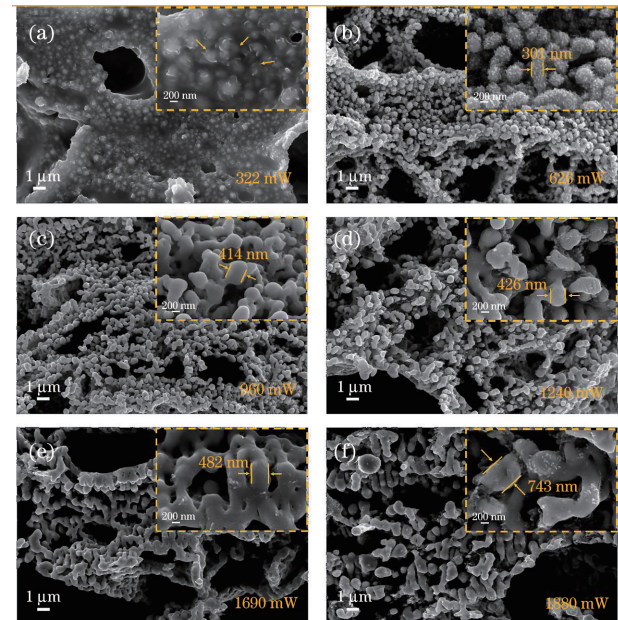


图3 飞秒激光不同激光功率下得到的铜微结构的SEM图  
(插图:高倍SEM图)。(a) 322 mW; (b) 626 mW;  
(c) 960 mW; (d) 1240 mW; (e) 1690 mW;  
(f) 1880 mW

Fig. 3 SEM images of copper microstructure obtained under different laser power(insets: high-resolution SEM images). (a) 322 mW; (b) 626 mW; (c) 960 mW; (d) 1240 mW; (e) 1690 mW; (f) 1880 mW

至426 nm[图3(d)]。随着激光功率进一步增大,辐照区域激光能量密度增大,Cu纳米颗粒间隙处热输入升高,导致颗粒间熔化程度提高,铜微结构中开始出现较大球形结构,如图3(e)~(f)所示。飞秒激光由于其超短脉宽,与纳米颗粒主要发生非热作用,所以Cu纳米颗粒形成的网络结构未出现大面积熔化结构。

利用HRTEM对所制备铜微结构的微观结构进行表征,进一步探究Cu纳米颗粒的连接过程。如图4(a)所示,还原得到的Cu纳米颗粒平均直径大约为24 nm。所标定的20.7 nm及20.9 nm对应于Cu的(111)晶面,通过激光诱导表面等离激元效应可实现Cu纳米颗粒的连接,如图4(b)所示。同时,基于PVP的分解可形成约3 nm碳层包裹于Cu表面<sup>[20-24]</sup>。由于激光对Cu<sup>2+</sup>的不完全还原,铜微结构中同样存在部分Cu<sub>2</sub>O。所标定的24.2 nm晶面间距对应于Cu<sub>2</sub>O(111)晶面,如图4(c)、(d)所示。这些Cu<sub>2</sub>O与Cu之间的连接界面明显,如图中箭头所示。在Cu<sub>2</sub>O及Cu的表面也可观察到明显的碳层结构,该碳层与铜之间未观察到良好冶金结合,表明这些碳层通过范德瓦尔斯力包裹于铜表面形成包覆结构。

### 3.3 激光辐照下铜纳米颗粒二聚体的温度场分布

利用COMSOL模拟了飞秒激光辐照下Cu纳

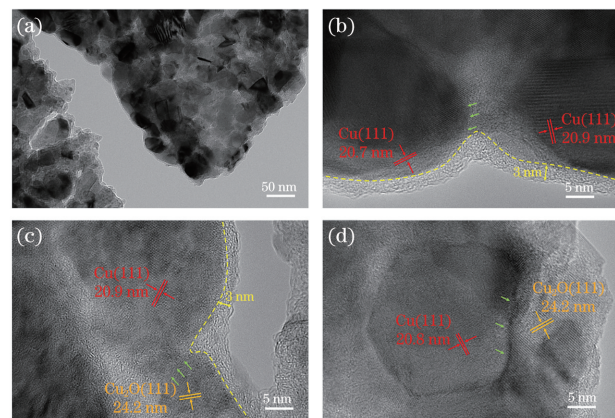


图4 960 mW 激光功率下得到的铜微结构的HRTEM图。(a) Cu纳米颗粒;(b) Cu纳米颗粒连接界面及Cu-C界面;(c)(d) Cu-Cu<sub>2</sub>O纳米颗粒连接界面

Fig. 4 HRTEM images of the copper microstructure obtained at 960 mW laser power. (a) Cu nanoparticles; (b) interfaces of Cu nanoparticles and Cu-C structure; (c) (d) interfaces of Cu-Cu<sub>2</sub>O nanoparticles

米颗粒二聚体周围的电场及温度场分布特征,进一步探究Cu纳米颗粒的连接机理。激光脉冲宽度设置为50 fs,激光波长为800 nm,Cu纳米颗粒半径为155 nm[统计自图3(a)中的Cu纳米颗粒],设定颗粒间距为6 nm。Cu纳米颗粒二聚体的几何模型如图5(a)所示。图中最外层灰色的区域表示完美

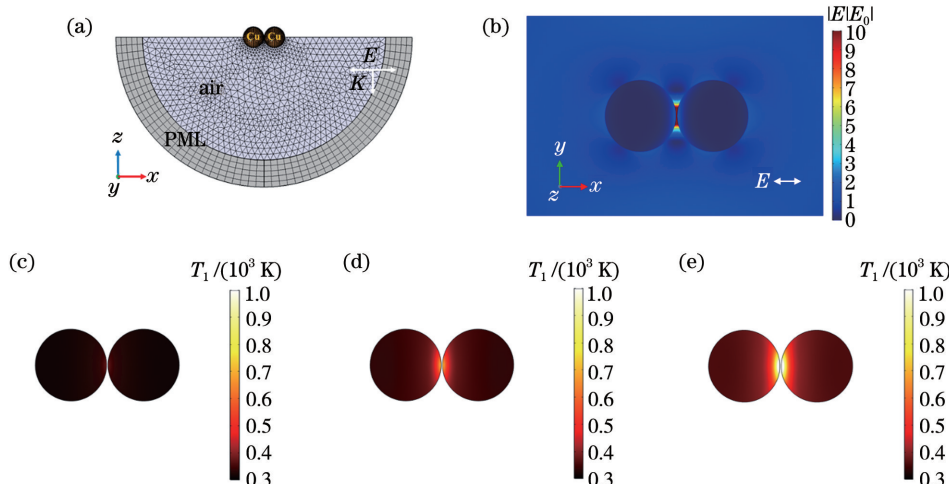


图5 飞秒激光辐照铜纳米颗粒二聚体COMSOL仿真模拟结果。(a)Cu纳米颗粒二聚体的几何模型示意图;(b)960 mW激光辐照下Cu纳米颗粒二聚体的相对电场增强( $|E/E_0|$ )分布,其中 $E$ 为计算出的电场强度, $E_0$ 为入射电场强度;(c)~(e)322 mW,960 mW,1690 mW的单脉冲激光辐照下,Cu纳米颗粒二聚体在5 ps时间后的温度场分布

Fig. 5 COMSOL simulation results of femtosecond laser irradiation of a Cu nanoparticle dimer. (a) Schematic of the model geometry for a Cu nanoparticles dimer; (b) relative electric field enhancement ( $|E/E_0|$ ) distribution of the Cu nanoparticle dimer under 960 mW laser irradiation, where  $E$  is the calculated electric field intensity and  $E_0$  is the incident electric field intensity; (c)–(e) temperature field distribution of a Cu nanoparticle dimer under 322 mW, 960 mW, and 1690 mW single pulse laser irradiation after 5 ps, respectively

匹配层(PML),以截断电磁域,并减少来自边界的波反射。紫色域为模拟的空气域,橙色域显示了Cu纳米颗粒的几何形状。入射电场沿x轴线性极化,平行于z轴负方向传播。图5(b)为960 mW激光辐照下,Cu纳米颗粒二聚体的电场分布特征。图中显示,在激光辐照下,Cu纳米颗粒表面电荷出现极化现象在颗粒两侧聚集,并且电荷极化方向与入射激光偏振方向平行。当激光偏振方向与纳米颗粒二聚体轴向平行时,纳米结构的相对电场增强最大值( $|E/E_0|=34.7$ )在纳米颗粒间隙处产生。进一步,对比了不同功率的单脉冲飞秒激光辐照下,Cu纳米颗粒二聚体的晶格温度场分布(采样自激光辐照Cu纳米颗粒后5 ps),如图5(c)~(e)所示。不同激光功率下,Cu纳米颗粒均存在热区及冷区的分布。该纳米结构的晶格“热点”位置出现在颗粒间隙处,对应于纳米结构的相对电场增强最大的位置,如图5(b)所示。这证明了,在激光辐照Cu纳米颗粒二聚体时,表面等离激元效应倾向于在颗粒间隙处聚集产生,在颗粒间隙处产生最大的场强,导致该区域具有高的能量吸收效率,从而促进纳米颗粒的局部加热,实现颗粒互连。随着激光功率的升高,纳米颗粒“热点”区域的温度显著升高,如图5(c)~(e)所示。

进一步,利用双温模型计算了不同功率的单脉冲激光辐照下,Cu纳米颗粒电子及晶格温度随时间变化规律,如图6所示[模拟点取自图5(c)~(e)的纳米颗粒二聚体间隙热点区域]。当激光作用于Cu纳米颗粒二聚体时,间隙位置处电子温度( $T_e$ )急剧

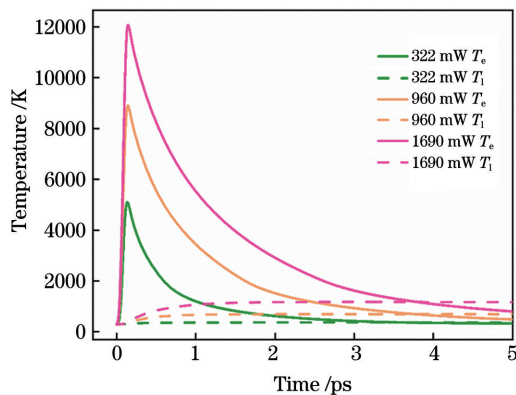


图6 不同功率的单脉冲激光辐照下,前5 ps内Cu纳米颗粒的电子及晶格温度随时间变化关系图

Fig. 6 Relationship between electron and lattice temperature of Cu nanoparticles in the first 5 ps under different laser powers of single pulse laser irradiation

升高且其最高温度远远大于晶格温度( $T_l$ )。随着激光功率升高,Cu颗粒的 $T_e$ 及 $T_l$ 温度显著升高,且激光功率越高,其 $T_e$ 与 $T_l$ 间的温度差异越大。当激光功率为322 mW时, $T_e$ 及 $T_l$ 的峰值温度分别为5099 K及371 K,在 $t=3.6$  ps时,晶格和电子温度相等。此后, $T_e$ 继续降低而低于 $T_l$ ,这是由于电子向更深位置的电子传热,此效应强于电子和晶格间的热量交换,导致 $T_e$ 和 $T_l$ 间出现非平衡状态<sup>[25]</sup>。当激光功率增至960 mW时, $T_e$ 及 $T_l$ 的峰值温度分别升高至8899 K及698 K。而当激光功率进一步增至1690 mW时, $T_e$ 的峰值温度增至12068 K, $T_l$ 的峰值温度增至1175 K。其中,对于不同激光功率辐照下的纳米颗粒,其最大晶格温度均低于铜块体的熔点(1357 K)<sup>[15]</sup>。由于纳米颗粒的表面效应及尺寸效应,纳米颗粒的整体熔化温度比块状材料的熔化温度低,且颗粒表面的原子易发生扩散<sup>[21]</sup>。研究表明,Cu纳米颗粒在500 K左右低温下即可发生表面熔化,促进纳米颗粒间的连接<sup>[26]</sup>。因此,当激光功率为322 mW时,Cu纳米颗粒间隙处晶格温度最高为371 K,颗粒表面不会出现熔化现象,无法实现连接。当激光功率为960 mW时,晶格温度最高达698 K,推测纳米颗粒已出现表面熔化现象,可实现颗粒间的连接。而当激光功率增至1690 mW时,晶格温度最高增至1175 K,推测纳米颗粒熔化程度更大,颗粒连接程度将进一步提高。对比实验结果,在322 mW的激光功率下,仅观察到分散的Cu纳米颗粒,颗粒之间未实现连接,如图3(a)所示;激光功率为960 mW时,Cu纳米颗粒完全连接形成网络状结构,如图3(c)所示;当激光功率进一步增至1690 mW时,Cu纳米颗粒连接程度提高,烧结颈尺寸增大至482 nm,如图3(e)所示。模拟结果与实验结果符合良好。

## 4 结 论

本文利用飞秒激光扫描铜离子前驱体,原位还原并连接铜纳米颗粒,成功制备了具有良好导电性能的铜微结构。当激光功率为960 mW、扫描速率为3 mm/s时,制备的铜微结构方阻最低达 $11.2 \Omega \cdot \text{sq}^{-1}$ 。利用COMSOL软件建立了单脉冲飞秒激光作用下的双温模型,模拟了激光辐照下Cu纳米颗粒二聚体周围的电场及温度场分布,计算了不同激光功率下纳米颗粒热区的电子及晶格温度随时间的变化关系。当激光辐照纳米颗粒二聚体时,

激光诱导的等离激元效应可实现对颗粒的局域加热,从而使纳米颗粒发生互连。随着激光功率的升高,纳米颗粒间隙热区的晶格温度升高,颗粒间连接程度提高。当激光功率为 960 mW 时,晶格最高温度为 698 K,纳米颗粒出现表面熔化现象,可实现颗粒间的连接。仿真结果与实验结果符合良好,为飞秒激光辐照下铜纳米颗粒的连接机理提供了实验及理论依据。

## 参 考 文 献

- [1] Hu A, Zhou Y, Duley W W. Femtosecond laser-induced nanowelding: fundamentals and applications [J]. *The Open Surface Science Journal*, 2011, 3(1): 42-49.
- [2] Zhong M L, Fan P X. Applications of laser nano manufacturing technologies [J]. *Chinese Journal of Lasers*, 2011, 38(6): 0601001.  
钟敏霖, 范培迅. 激光纳米制造技术的应用[J]. 中国激光, 2011, 38(6): 0601001.
- [3] Ravi Kumar D V, Woo K, Moon J. Promising wet chemical strategies to synthesize Cu nanowires for emerging electronic applications [J]. *Nanoscale*, 2015, 7(41): 17195-17210.
- [4] Wang S, Tian Y H. The state of art on the micro-joining and nano-joining technologies [J]. *Materials Science and Technology*, 2017, 25(5): 1-5.  
王尚, 田艳红. 微纳连接技术研究进展[J]. 材料科学与工艺, 2017, 25(5): 1-5.
- [5] Gao F, Gu Z. Nano-soldering of magnetically aligned three-dimensional nanowire networks [J]. *Nanotechnology*, 2010, 21(11): 115604.
- [6] Chang B H, Zhou Y. Numerical study on the effect of electrode force in small-scale resistance spot welding [J]. *Journal of Materials Processing Technology*, 2003, 139(1/2/3): 635-641.
- [7] Xiao M, Zheng S, Shen D Z, et al. Laser-induced joining of nanoscale materials: processing, properties, and applications [J]. *Nano Today*, 2020, 35: 100959.
- [8] Deng Y B, Bai Y F, Yu Y C, et al. Laser nanojoining of copper nanowires [J]. *Journal of Laser Applications*, 2019, 31(2): 022414.
- [9] Sobolev S L. Nonlocal two-temperature model: application to heat transport in metals irradiated by ultrashort laser pulses [J]. *International Journal of Heat and Mass Transfer*, 2016, 94: 138-144.
- [10] Shi Y, Xu B, Wu D, et al. Research progress on fabrication of functional microfluidic chips using femtosecond laser direct writing technology [J]. *Chinese Journal of Lasers*, 2019, 46(10): 1000001.  
史杨, 许兵, 吴东, 等. 飞秒激光直写技术制备功能化微流控芯片研究进展[J]. 中国激光, 2019, 46(10): 1000001.
- [11] Roth G L, Haubner J, Kefer S, et al. Fs-laser based hybrid micromachining for polymer micro-opto electrical systems [J]. *Optics and Lasers in Engineering*, 2021, 137: 106362.
- [12] Huang H, Liu L, Peng P, et al. Controlled joining of Ag nanoparticles with femtosecond laser radiation [J]. *Journal of Applied Physics*, 2012, 112(12): 123519.
- [13] Huang H, Sivayoganathan M, Duley W W, et al. High integrity interconnection of silver submicron/nanoparticles on silicon wafer by femtosecond laser irradiation [J]. *Nanotechnology*, 2015, 26(2): 025303.
- [14] Anisimov S I, Kapeliovich B L, Perel'man T L. Electron emission from metal surfaces exposed to ultra-short laser pulses [J]. *Zhurnal Eksperimental'noi Teroreticheskoi Fiziki*, 1974, 66(776): 776-781.
- [15] Cheng C W, Chen J K. Femtosecond laser sintering of copper nanoparticles [J]. *Applied Physics A*, 2016, 122(4): 1-8.
- [16] Liao J N, Wang X D, Zhou X W, et al. Femtosecond laser direct writing of copper microelectrodes [J]. *Chinese Journal of Lasers*, 2019, 46(10): 1002013.  
廖嘉宁, 王欣达, 周兴汶, 等. 飞秒激光直写铜微电极研究[J]. 中国激光, 2019, 46(10): 1002013.
- [17] Han S, Hong S, Ham J, et al. Fast plasmonic laser nanowelding for a Cu-nanowire percolation network for flexible transparent conductors and stretchable electronics [J]. *Advanced Materials*, 2014, 26(33): 5808-5814.
- [18] Zhai H T, Wang R R, Wang X, et al. Transparent heaters based on highly stable Cu nanowire films [J]. *Nano Research*, 2016, 9(12): 3924-3936.
- [19] Zhou X W, Guo W, Zhu Y, et al. The laser writing of highly conductive and anti-oxidative copper structures in liquid [J]. *Nanoscale*, 2020, 12(2): 563-571.
- [20] Lee H, Yang M Y. Effect of solvent and PVP on electrode conductivity in laser-induced reduction process [J]. *Applied Physics A*, 2015, 119(1): 317-323.
- [21] Hu A, Peng P, Alarifi H, et al. Femtosecond laser welded nanostructures and plasmonic devices [J]. *Journal of Laser Applications*, 2012, 24(4): 042001.
- [22] Lin L, Huang H, Sivayoganathan M, et al. Assembly of silver nanoparticles on nanowires into ordered nanostructures with femtosecond laser

- radiation[J]. Applied Optics, 2015, 54(9): 2524-2531.
- [23] Davletshin Y R, Kumaradas J C. The role of morphology and coupling of gold nanoparticles in optical breakdown during picosecond pulse exposures [J]. Beilstein Journal of Nanotechnology, 2016, 7: 869-880.
- [24] Wang S L, Huang X L, He Y H, et al. Synthesis, growth mechanism and thermal stability of copper nanoparticles encapsulated by multi-layer graphene [J]. Carbon, 2012, 50(6): 2119-2125.
- [25] Ren Y P, Chen J K, Zhang Y W. Optical properties and thermal response of copper films induced by ultrashort-pulsed lasers [J]. Journal of Applied Physics, 2011, 110(11): 113102.
- [26] Li Q B, Wang M, Liang Y P, et al. Molecular dynamics simulations of aggregation of copper nanoparticles with different heating rates[J]. Physica E: Low-Dimensional Systems and Nanostructures, 2017, 90: 137-142.

## Joining Process of Copper Nanoparticles with Femtosecond Laser Irradiation

Liao Jianing, Wang Xinda, Zhou Xinwen, Kang Hui, Guo Wei, Peng Peng\*

*School of Mechanical Engineering & Automation, Beihang University, Beijing 100191, China*

### Abstract

**Objective** Copper (Cu) nanoparticle exhibits high potential as an interconnecting material in electronic devices due to its relatively lower cost and similar conductivity compared with other noble metals. The interconnection between Cu nanoparticles can optimize the electrical conductivity and optical and mechanical properties of fabricated Cu microstructures. Compared with other traditional joining technologies, laser-induced nanojoining has the advantages of high precision, low damage, and high efficiency. In particular, femtosecond lasers with high peak power and ultrashort pulse duration would limit the heat-affected zone and result in less damage of joint than other lasers with longer pulse duration or continuous wave. When femtosecond laser pulse interacts with metallic nanomaterials, electrons absorb photons and quickly reach a higher temperature, while the lattice remains unchanged, resulting in less thermal effect and local melting during processing. It is expected to have potential in joining materials at nanoscale. At present, some reports focus on the reduction of Cu nanoparticles by femtosecond laser irradiation, whereas the effect of femtosecond laser on the joining process of Cu nanoparticles is yet to be understood. The joining mechanism and laser thermal effect on the joining of Cu nanoparticles need to be given more effort to optimize the femtosecond laser processing. In this work, femtosecond laser direct-writing is used to *in-situ* reduce Cu nanoparticles and join them to form a conductive copper microstructure. The effect of laser power on the composition, microstructure, and conductivity of Cu microstructures are investigated. Furthermore, the effect of single-shot laser pulses on the electron and lattice temperature in the “hotspot” between a Cu nanoparticle dimer is calculated. Simulation experimental results are compared to understand the joining process and mechanism of Cu nanoparticles under femtosecond laser irradiation.

**Methods** In a typical experimental procedure, the aqueous solution of polymethacrylic acid sodium salt (PMAA-Na, 30%, 1  $\mu$ L), and polyvinyl pyrrolidone (PVP, 0.25 g/mL, 1200  $\mu$ L) are added to the aqueous solution of copper nitrate hydrate ( $\text{Cu}(\text{NO}_3)_2 \cdot 3\text{H}_2\text{O}$ , 1.208 g/mL, 1000  $\mu$ L) to form a Cu ion precursor. The as-prepared Cu ion precursor (200  $\mu$ L) is coated on a polycarbonate flexible substrate (PC, 2.5 cm  $\times$  5 cm) and then dried at 50 °C in an oven. The femtosecond laser is used to scan the dry precursor film to reduce Cu ion to Cu nanoparticles and join the nanoparticles to form a conductive Cu microstructure. After laser writing, deionized water is used to clean the Cu microstructure to leave the as-written structures on a substrate. The electrical properties of the Cu microstructure are measured with a source meter using the four-point probe method. Then, the morphology of the Cu microstructure is characterized by field emission scanning electron microscopy and high-resolution transmission electron microscopy. X-ray diffraction is used to verify the chemical composition of the Cu microstructure. The effect of laser power on the chemical composition, microstructure, and conductivity of Cu are studied. Finally, the electric field and temperature field distribution characteristics of the Cu nanoparticle dimer under femtosecond laser irradiation are simulated using COMSOL Multiphysics, and the effect of single-shot laser pulses on the electron and

lattice temperature of Cu nanoparticles is calculated.

**Results and Discussions** The sheet resistance of as-fabricated Cu microstructure presents a tendency to decrease first and then slowly increase with the increase of laser power (Fig.1). The Cu microstructure obtained at 960 mW laser power exhibits the lower sheet resistance of  $11.2 \Omega \cdot \text{sq}^{-1}$ . When the laser power is 322 mW, insufficient laser energy input results in the reduction of only a few dispersed Cu nanoparticles from the precursor, leading to high sheet resistance. As the laser power increases to 960 mW, more Cu nanoparticles are reduced and joined to form a dense network structure because of more hot-spots induced by the plasmonic effect, which greatly enhances its conductivity (Fig.3). Further increasing the laser power to 1690 mW or above, the high local temperature can melt Cu nanoparticles to form large micron-sized Cu, resulting in the increased sheet resistance. The simulation results show that the lattice temperature at the contact area of the Cu nanoparticle dimer increases as the incident laser power increases (Fig.5). When the laser power is 960 mW, the lattice temperature of the “hotspot” between the Cu nanoparticle dimer is up to 698 K. It induces surface melting of Cu nanoparticles and facilitates their interconnection (Fig.6). As the laser power increases to 1690 mW, the lattice temperature increases to 1175 K, resulting in intensive melting and interconnection of nanoparticles. These also have been observed in the experiment.

**Conclusions** In this work, femtosecond laser direct-writing was used to reduce Cu nanoparticles and *in-situ* joins them to fabricate the Cu microstructure with high conductivity. The Cu microstructure obtained at 960 mW laser power and 3 mm/s scan rate exhibited the lowest sheet resistance of  $11.2 \Omega \cdot \text{sq}^{-1}$ . A two-temperature model during single-pulse femtosecond laser irradiation was employed to calculate the electron and lattice temperature of Cu nanoparticles using COMSOL Multiphysics. Laser-induced localized surface plasmon effect on the Cu nanoparticle dimer enhanced the local temperature greatly at the contact area of Cu nanoparticles, contributing to the interconnection of nanoparticles. As the incident laser power increased, the lattice temperature at the contact area of the Cu nanoparticle dimer increased, leading to intensive joining. When the laser power was 960 mW, the lattice temperature of the “hotspot” between the Cu nanoparticle dimer was up to 698 K, which can cause surface melting to facilitate joining. The consistent experimental and simulation results provide a further understanding of the joining process and mechanism of Cu nanoparticles under femtosecond laser irradiation.

**Key words** laser technology; femtosecond laser; copper nanoparticles; nano-joining; interface; local temperature

**OCIS codes** 140.3390; 140.3450; 230.4000